Structure-based mutagenesis of phycobiliprotein smURFP for optoacoustic imaging

Juan Pablo Fuenzalida Werner[a], Kanuj Mishra[a], Yuanhui Huang[a,c], Paul Vetschera[a,c], Sarah Glasl[a], Andriy Chmyrov[a,c,d], Klaus Richter[b], Vasilis Ntziachristos[a,c,d] and Andre C. Stiel[a]*

a) *Institute of Biological and Medical Imaging (IBMI), Helmholtz Zentrum München, Neuherberg, Germany*
b) *Center for Integrated Protein Science, Department of Chemistry, Technische Universität München, Garching, Germany*
c) *Chair of Biological Imaging, Technische Universität München, Munich, Germany*
d) *Center for Translational Cancer Research (TranslaTUM), Technische Universität München, Munich, Germany*
*) *Correspondence should be addressed to A.C.S. (andre.stiel@helmholtz-muenchen.de)*

ABSTRACT

Photo- or optoacoustics (OA) imaging is increasingly used as a non-invasive imaging method that can simultaneously reveal structure and function in deep tissue. However, the most frequent transgenic OA labels are current fluorescent proteins not optimized for OA imaging. Thus, they lack in OA signal strength and their absorption maxima are positioned at short wavelength, thus with low penetration depth and high background signal. Here we apply insights from our recent structure determination of the fluorescent phycobiliprotein smURFP to mutate a range of residues to promote the non-radiative decay pathway that generates OA signal. We identified hydrophobic and aromatic substitutions within the chromophore-binding pocket that substantially increase OA signal and red-shift the absorption. Our results demonstrate the feasibility of structure-based mutagenesis to re-purpose fluorescent probes for OA imaging, and they may provide structure-function insights for de novo engineering of transgenic OA probes.

INTRODUCTION

Optoacoustic (OA) imaging shows potential for non-invasive studies of biological function but is limited by the availability of suitable OA labels that allow imaging of specific processes at the cellular and sub-cellular level [1–3]. Fundamentally, any absorbing material can serve as an optoacoustic label, but preferred characteristics include a high absorption (extinction) coefficient, low quantum yield (Φ_{fl}), and high photostability. Also desired is strong absorption in the near-infrared spectral region (~650 – 950 nm), which reduces scattering and interference with endogenous chromophores (e.g. blood hemoglobin and melanin). In addition, OA labels should be optimized to avoid fluorescence and other relaxation mechanisms that can compete with non-radiative decay [4–6]. In addition to these characteristics, OA labels should ideally be

genetically encoded, which allows longitudinal *in vivo* studies of developmental processes [7] or of tumor growth and treatment [8].

Relatively few transgenic OA labels have been described, and research in this area has focused on dye synthesis [9–11], green fluorescent protein (GFP)-like fluorophores with reduced Φ_{fl} [12], as well as far-red bacteriophytochrome proteins [13], including their switchable variants [14,15]. Another class of far-red absorbing proteins not considered for OA imaging so far are phycobiliproteins (PBPs). These proteins, naturally found as light-harvesting complexes in photosynthetic bacteria, form ring-shaped, high-molecular-weight aggregates containing several tetrapyrrole-based chromophores [16]. Recently the laboratory of the late Roger Tsien replaced the natural phycocyanobilin chromophore of the allophycocyanin from *Trichodesmium erythraeum* (α subunit) with biliverdin (BV), a product of the heme degradation pathway in mammalian cells. The result was smURFP, a dimeric 30 kDa label with an absorption peak at 642 nm and emission peak at 670 nm [17]. More recently, Zhao and coworkers reported another PBP with BV binding capability, termed BDFP, which absorbs around 680 nm [18]. BDFP binds BV more efficiently than smURFP does, but shows approximately 50% lower absorptivity. Fluorescence imaging experiments showed that both smURFP and BDFP can be expressed in functional form in mammalian cell lines.

Three factors make PBPs promising candidates for optoacoustic labels: i) native PBPs have a high chromophore-to-protein ratio, such that each chromophore corresponds to ~ 8 kDa, much smaller than the ~ 20 kDa per chromophore for a minimal bacteriophytochrome [19]; ii) they show comparatively high resistance to photo-fatigue, so they tolerate the high-energy laser doses required for OA imaging; and iii) they occur naturally as high-molecular-weight aggregates, a tendency that could be harnessed to produce inert absorbing clusters in cells. Such aggregates are not a preferred choice in fluorescence imaging applications, as they may quench fluorescence emission, but they are advantageous in OA imaging because they offer a larger absorption cross-section, resulting in stronger OA signal.

With a Φ_{fl} of 0.18 smURFP is optimized for fluorescence emission, and it absorbs maximally at wavelengths shorter than 650 nm, where background OA signal from endogenous absorbers is relatively strong which renders the protein unsuitable for OA. We hypothesized that we could introduce mutations in the vicinity of the BV chromophore in order to make the protein suitable for OA imaging. Based on our recent structures of an apo-smURFP variant (PDB 6FZO) and a smURFP variant bound to BV (6FZN) [20], we used site-directed mutagenesis to improve protein for OA imaging. We identified hydrophobic and aromatic substitutions within the chromophore-binding pocket that increased OA signal by up to 50% and red-shifted the absorption by up to 30 nm. Our results demonstrate the feasibility of structure-based mutagenesis to re-purpose smURFP, and potentially other PBPs, as labels for OA imaging.

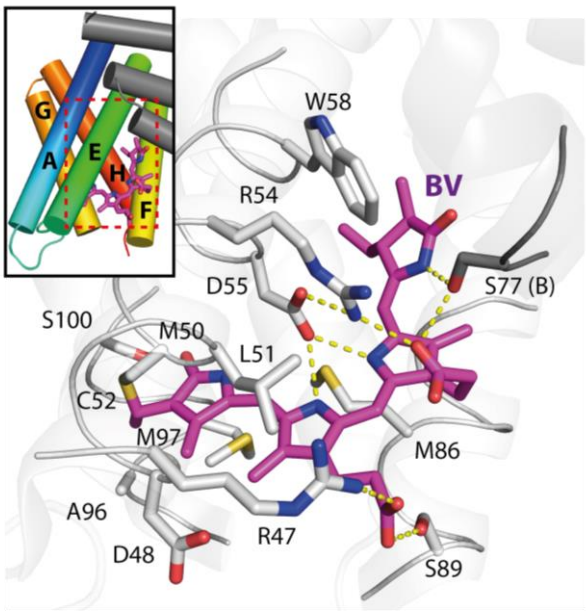

Figure 1: Crystal structure of a smURFP-Y56R mutant covalently bound to BV chromophore (PDB 6FZN). The overall structure including helix naming is shown as an insert, with the dashed line defining the region shown in the main figure panel. BV chromophore, bonded to the C52, is shown in magenta together with major interacting residues and residues addressed in this study. Monomer A and B are shown in different shades of grey. Major hydrogen bonds and electrostatic interactions are indicated as dotted lines.

METHODS

Chemicals: BV was purchased from Frontier Scientific. All other chemicals used for buffer preparation were purchased from Sigma-Aldrich. Proteins were purified into phosphate-buffered saline (PBS), which was also the diluent used in all experiments.

Cloning and mutagenesis: The coding sequence of *T. erythraeum* smURFP (Genbank KX449135.1) was subcloned into the multiple cloning site of pET-Duet1 (Novagene) using *NdeI* and *XhoI*. The coding sequence of heme oxygenase of *Nostoc sp.* (a kind gift from A. Möglich) was cloned into the site immediately upstream using *NcoI* and *HindIII*. Site-specific mutants of smURFP were generated using the QuikChange Lightning Mutagenesis Kit (Agilent Technologies) according to the manufacturer's instructions and confirmed by standard DNA-sequencing.

Protein Expression: Proteins were expressed in *Escherichia coli* BL21 and purified by Ni-NTA affinity chromatography, followed by gel filtration on a HiLoad 26/600 Superdex 75pg column (Amersham Biosciences). Purified proteins were frozen immediately in liquid nitrogen and stored at –80 °C. Thawed proteins were centrifuged at 14,000 rpm for 45 min at 4°C, and supernatant was used in measurements. Variants of smURFP not covalently bound to BV were mixed with BV in 2-fold molar excess of protein in order to ensure that all BV molecules were bound (Supplementary Figure 2).

Absorption and Fluorescence Spectroscopy: UV-VIS measurements were performed using a UV-1800 spectrophotometer (Shimadzu) in 100 µl quartz cell with a path length of 1 cm. The extinction coefficients were calculated assuming that the extinction coefficient of the holo-protein at 388 nm was equal to that of free BV in PBS (39,900 $M^{-1} \cdot cm^{-1}$)[21]. Fluorescence measurements were performed with a Cary Eclipse Fluorescence spectrophotometer (Varian). The excitation wavelength was fixed at 646 nm, and emission

and excitation slits were set to 5 nm. The absorbance at the excitation wavelength was always equal to 0.1 to avoid inner filter effects.

OA Spectroscopy: Samples with absorbance between 0.07 and 0.35 at 680 nm were measured using a real-time multispectral optoacoustic tomography (MSOT) system (inVision 256, iThera Medical) as described [22]. The sample holder was designed to hold two, 1-ml syringes. One syringe contained reference solution of India ink and the other contained the sample. Three samples with increasing concentration were measured for each variant and for methylene blue. We defined a region of interest (ROI) in the resulting MSOT images, extracted average signal per ROI for the reference and sample separately, and normalized the average signal of the sample based on the reference. We adjusted the normalized average signal of the sample to the signal obtained with the corresponding concentration of methylene blue, in order to enable comparisons between measurement sessions (see Supplementary figure 1). Methylene blue is a well-established OA label of tumors and lymphatic vessels [23].

Selected samples were also analyzed using a dedicated optoacoustic spectroscopy system that we developed[24]. OA signals were generated using a pulsed nanosecond optical parametric oscillator (OPO) laser (Spitlight-DPSS 250 ZHG-OPO) with pulse repetition rate of 50 Hz. Constant pulse energy was ensured using a combination of half wave plate controlled by a motorized rotation stage (PRM1Z8) and a polarizing beam splitter. Samples were injected into an acoustically coupled, hydrophobic, uncoated µ-Slide I 0.2 Luer flow chip (IBIDI) and illuminated from one side using a fiber bundle. OA signals were detected using a single-element 3.5-MHz transducer (V382-SU, Olympus). A second flow chip in the illumination path containing India ink at low concentration was used as a reference OA signal to correct for laser fluctuation during the measurement.

Analytical Ultracentrifugation: Analytical ultracentrifugation was performed on an XL-I analytical ultracentrifuge (Beckman). Proteins and BV were tracked based on absorption at 280, 387 and 677 nm, which provided information not only on their respective concentrations but also on their binding. Sedimentation runs were performed at 42,000 rpm in PBS at 20 °C.

Binding affinity of smURFP variants to BV was determined in titration experiments. BV at a constant concentration of 25 µM was mixed with seven concentrations (0–75 µM) of each smURFP variant. Absorbance was measured at 387 nm to determine the fraction of BV bound prior to ultracentrifugation provided information about the fraction of free BV, while absorbance at 387 nm during ultracentrifugation gave information about the fraction of bound BV. These values were then fit to a single-site-binding model.

Animal Imaging: MSOT was used to image implants of Matrigel containing bacteria expressing smURFP variants in mice *in vivo*. All animal experiments were approved by the Government of Upper Bavaria and were carried out in accordance with institutional and local guidelines. The animals were anesthetized using 2% isoflurane in O_2. Phenol red-free Matrigel

(catalog no. 354262, Corning) was mixed with an equal volume of *E. coli* B21 expressing the desired smURFP implant, and 40 µl of the mixture was injected into the back of FoxN1 nude mice (Charles River Laboratories) using a 30-gauge 1 ml syringe. The animals were placed in the MSOT holder using ultrasound gel and water as coupling media. The entire back of the mouse was imaged in slices 500 µm apart at wavelengths from 680 nm to 960 nm in 10 nm steps. Mice were sacrificed immediately after the measurement while still under anesthesia.

After filtering the data for signals between 0.1 and 7 MHz, MSOT images were reconstructed using a model-based linear approach[25] with a field-of-view (FOV) of 332 x 332 pixels and a pixel resolution of 75 x 75 µm. Pixels showing the spectrum of smURFP-Y56L were unmixed using orthogonal subspace projection in Matlab (R2018A, MathWorks) together with spectral information of smURFP-Y56L obtained with the OA spectrometer (see above). False color images indicate confidence levels of unmixing. The spectra obtained from the MSOT images are the mean spectra of all unmixed pixels

RESULTS AND DISCUSSION

We explored structural based mutagenesis of smURFP involving covalent and non-covalent complexes with BV. In both cases, the tetrapyrrole chromophore is stabilized in a binding pocket between helices E and F by a conserved Arg-Asp pair (Figure 1). In the case of PBPs bound covalently to their chromophore, a Cys in helix E lying upstream of the Arg-Asp (R54, D55) pair bonds with the chromophore[26–28]; this residue is Cys52 in *T. erythraeum* smURFP and Cys84 in the consensus PBP sequence[27,28]. This Cys is usually a Ser in PBPs with non-covalently bound chromophores[29].

Mutants of smURFP bound non-covalently to BV. We were particularly interested in optimizing non-covalent smURFP:BV complexes for OA imaging. Since non-covalently bound BV retain one extra double bond, an increase in conjugation could lead to an absorption red shift. This phenomena has been describe in bacterial phytochromes[30]. In addition, the greater rotational and vibrational freedom of the non-covalently bound tetrapyrrole leads to generally lower Φ_{fl} compared to covalently attached chromophores [29], which is directly connected to improved photostability and smaller ground state depopulation as describe for FPs derived from *Discosoma sp*. [5]. Both characteristics are favorable for OA labels.

Many organic dyes and pigments[31,32], including BV[33,34], show a bathochromic shift and / or increased absorptivity in hydrophobic surroundings. Therefore, we explored replacing the chromophore-binding Cys52 and surrounding residues with aromatic and other hydrophobic amino acids. In smURFP a major portion of the chromophore binding pocket is already occupied by large hydrophobic residues (L51, W58, F59, F65, M86; Figure 1). Thus, we focused our attention on mutations at positions C52, R56, A96, M97, S100 and I101 or combinations thereof, in order to increase the hydrophobicity of the binding pocket.

The Optoacoustic signal (OaS) is the pressure rise produced by the non-radiative energy decay from an excited state, and it is classically described by equation (1)[35] ,

$$p_0 = \Gamma \mu_a \Phi (1 - \Phi_{fl}) \qquad (1)$$

where μ_a is the local optical absorption coefficient, Φ is the light fluence, and Φ_{fl} is the fluorescence quantum yield. Γ is the dimensionless Grüneisen parameter, which represents the thermoelastic properties of the medium. This equation focuses on radiative decay as the only decay pathway competing with OA signal generation, and it ignores other photochemical processes such as transient photoisomerization, electron transfer or intersystem crossing (ISC)[4]. Normalizing OaS by the molecular concentrations, yields φP, which describes the molar efficiency of a molecule in converting light to OaS [22]. Alternatively, OaS can be normalized by the absorbance, resulting in the OA generation efficiency (photoacoustic generation efficiency, PGE) as a measure of how much of the absorbed energy is converted to pressure [4,6,36]. All radiative and non-radiative decay pathways that do not contribute to OA signal decrease PGE. For this reason, we wished to measure φP and PGE for the smURFP variants.

Table 1. Photophysical properties of wild-type and mutant smURFPs

Protein	λ_{max}	$\varepsilon_{peak}\cdot10^3$ $M^{-1}cm^{-1}$	$\varepsilon_{680nm}\cdot10^3$ $M^{-1}cm^{-1}$	λ_{em}+	Φ_{fl},% *	φP_{680nm}	PGE_{680nm}
Wild-type smURFP	644	168	25	668	18	1.3±0.1	2.1±0.1
Mutants bound non-covalently to BV							
C52A	690	73	68	n.d.	n.d.	3.7±0.2	2.6±0.1
C52L	694	71	63	n.d.	n.d.	3.0±0.2	2.4±0.1
C52I	700	65	55	n.d.	n.d.	2.4±0.1	1.9±0.2
C52F	690	58	53	n.d.	n.d.	2.1±0.2	2.2±0.1
C52S	690	54	50	n.d.	n.d.	2.3±0.1	2.2±0.1
C52I Y56F	701	63	53	n.d.	n.d.	2.6±0.6	2.2±0.5
C52I Y56F A96I	701	61	51	n.d.	n.d.	2.8±0.2	2.6±0.2
C52I Y56F M97F	701	62	52	n.d.	n.d.	3.1±0.1	2.7±0.1
C52I Y56F S100I	694	56	50	n.d.	n.d.	1.9±0.5	1.8±0.4
C52I Y56F I101F	701	64	53	n.d.	n.d.	2.2±0.2	1.8±0.1
Mutants bound covalently to BV							
Y56A	672	116	108	692	2.7	5.6±0.1	2.2±0.1
Y56V	674	112	100	699	1	4.6±0.1	2.1±0.1
Y56L	675	104	93	699	1.2	6.9±0.1	2.4±0.1
Y56I	679	98	92	699	1.1	4.5±0.1	2.1±0.1
Y56F	677	77	73	668	2.7	3.8±0.2	2.3±0.1
Y56S	672	121	110	694	2.3	6.3±0.1	2.3±0.1

Y56R	672	111	105	692	1.2	4.6±0.1	1.9±0.1
Y56H	657	107	89	668	6.3	3.6±0.1	2.0±0.1
Y56W	696	66	60	668	2.8	3.4±0.1	2.5±0.1
Y56F I42F	677	95	93	694	0.7	4.1±0.1	1.8±0.1
Y56L I42F	675	108	103	697	1.4	6.6±0.1	2.2±0.1
iRFP720§	700	95	61	700	10	4.6±0.1	3.3±0.1

n.a., not applicable; n.d., not determined; Φ_{fl} Fluorescent quantum yield; φP_{680nm} Optoacosutic molar efficiency at 680 nm; PGE_{680nm} Optoacoustic generation efficiency at 680 nm.

*) absorbance at λ_{ex} was fixed at 0.1

+) λ_{em} Emission maxima.

§) Data taken from ref. [37]

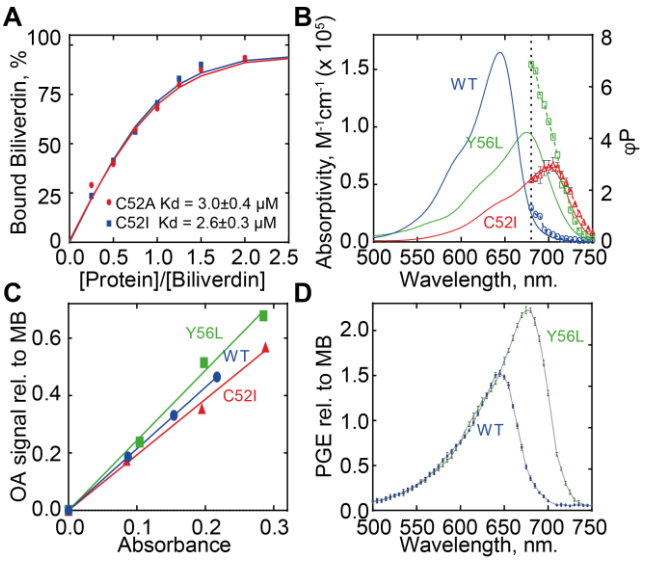

Figure 2: A) Analytical ultracentrifugation for smURFP variants C52A and C52I. Bound BV was calculated from the increase in BV sedimentation measured at 387 nm (Soret Band). Continuous lines represent best fitting with the quadratic binding model. **B**) Absorption spectra and MSOT derived OA molar efficiency of wildtype smURFP and non-covalent C52I and covalent Y56L. The dashed line indicates the beginning of the wavelength range useful for MSOT. **C**) OA signal intensity as a function of absorbance. Data were adjusted using measurements of reference solutions of methylene blue (MB). **D**) OA spectra measured with a custom build OA spectrometer of wild-type smURFP and variant Y56L. OA generation efficiency (PGE) relative to a reference solution of methylene blue (MB) was plotted as colored data points, connected by Gaussian best-fit lines (gray solid lines). Error bars show the standard deviation of OA signal averaged for 10 consecutive laser pulses at the same wavelength. PGE was calculated by dividing OA signal by peak absorption, as describe by Laufer et al. [36].

We purified all mutants using affinity and size-exclusion chromatography and recorded their absorption, fluorescence and OA spectral data after titration with BV at a protein:BV ratio of 2:1 (Table 1). When protein was added above this ratio, the

spectra did not change appreciably, suggesting that 2:1 was sufficient to ensure that each BV molecule was bound to a protein (Supplementary Figure 2).

All mutants of C52 showed a pronounced bathochromic shift relative to the wild-type protein, due to the extended π-electron system, with absorption peaks around 690 nm (Table 1). The most red-shifted single mutant was C52I, which showed a peak at 700 nm. (Complete spectra for all non-covalent mutant smURFP:BV complexes can be found in Supplementary Figures 3 and 4). Red shifts beyond the extension of the π-electron system for several of the hydrophobic substitutions could be explained by a solvophobic effect [38,39] or by an increase in conjugation due to a more strict chromophore planarity [26]. However, combining C52I with other hydrophobic mutations in the binding pocket did not significantly improve spectral properties further. All mutants showed a complete loss of fluorescence compared to wild-type smURFP, likely because the non-covalently bound BV is free to move and therefore able to dissipate the absorbed energy via non-radiative pathways. The mutants showed lower absorptivity (~ 100,000 M^{-1} cm^{-1}) than wild-type, which may mean that BV can bind in a way that leaves the chromophore more exposed to the polar solvent [40].

Absorbance titration curves of the C52 variants indicated no substantial changes in affinity of chromophore for the protein, despite the diversity of mutations (Supplementary Figure 2). In fact, the most blue-shifted non-covalent variant C52A and the most red-shifted C52I showed similar titration curves, as well as similar sedimentation profiles by analytical ultracentrifugation (Figure 2A). We conclude that mutations at position 52 in smURFP can substantially alter chromophore photophysics, without affecting its affinity for the protein. This result may help guide efforts to engineer smURFPs and potentially related proteins, such as PBPs, for OA imaging.

Next, we characterized all variants with absorbance maxima shifted towards the near-infrared (NIR), since these mutants may be particularly useful for OA imaging at wavelengths where background from endogenous absorbers (blood hemoglobin) is lower. We recorded OA signals using a commercial MSOT system with illumination from 680 to 960 nm; a spectral window favorable for *in vivo* measurements (Figure 2B and C). Despite their loss in absorptivity, several mutants showed higher φP_{680nm} (up to 3.7, for C52A) than wild-type, which can be mainly attributed to the loss of Φ_{fl} and the redshift of the absorption maxima. The linear relation between absorbance and optoacoustic signal (PGE) can be observed in figure 2C. PGE was similar across several mutant proteins (Table1), with exception of C52A, C52L and the two triple mutants, C52I-Y56F-A96I and C52I-Y56F-M97F, exhibited a PGE of ~ 2.6 compared to the PGE of 1.9 for the single C52I mutant, since PGE is independent of absorptivity and none of the mutants emitted detectable fluorescence, this increase must be related to other factors that foster OA signal generation. It is possible that the increased PGE in these mutants reflects reduced

transient isomerization and/or facilitation of the thermoelastic expansion responsible for generating the OA signal [6].

Overall our results suggest that structure-based mutagenesis can red-shift smURFP absorption by at least 40 nm, making the engineering of OA probes for use in the NIR range feasible.

Mutants of smURFP bound covalently to BV. The results with mutant smURFPs bound non-covalently to BV showed a pronounced red shift, but at the cost of molar absorptivity. Next, we attempted to red-shift absorption by mutating the binding pocket in smURFP bound covalently to BV. Mutations at several positions in the binding pocket showed negligible effect on the absorbance maxima of the bound BV (Figure 1, Table 1 and Supplementary Table 1). Only mutations at Y56 showed promising effects for OA signal generation, so we focused on hydrophobic substitutions at this position and on nearby residue 42.

Y56F showed a strong bathochromic shift from 644 nm (smURFP wild-type) to 677 nm. Surprisingly, a shift of similar degree was not observed when the same mutation was made in the smURFP variant non-covalently bound to BV, suggesting different chromophore binding modes between the covalent and non-covalent complexes. Interestingly, nearly all changes at position 56 had a strong influence on the spectra with bathochromic shifts of ~ 30 nm (Supplementary Figures 5 and 6); similar effects of Y56L have been described for Allophycocyanin B from *Synechocystis* bound to phycocyanobilin [26]. Y56H, the only one of our mutations that could potentially replace the tyrosine hydrogen-bonding capacity, showed the least pronounced shift of ~ 10 nm and the highest Φ_{fl}. Additionally, a correlation was observed between the magnitude of the bathochromic shift and hydrophobicity or aromatic character (W > I > F > L > V > A = S = R > H). Thus, one of the most hydrophobic and aromatic substitutions, Y56W, showed the largest bathochromic shift, with an absorption peak at 696 nm. Hydrophobic amino acids may establish more interactions with BV, including van der Waals, $\pi-\pi$ stacking, and hydrophobic interactions, leading to more extensive conjugation and reducing the energy of the electronic transition. These results are in accordance with the finding that red-shifted PBPs share not only the CXRD motif common to wild-type PBPs but an extended version of it, CXRDY/FGW, in which the chromophore is more planar because it is sandwiched between bulky side chains [26]. In smURFP this is the hydrophobic packing around the D-ring of BV by W58 and F59 and a further F of chain B (Supplementary Figure 7).

We found that all red-shifting substitutions at Y56 reduced absorptivity. In fact, the loss in absorptivity was greater with more hydrophobic/aromatic substitutions, which also gave greater red shifts. Again, Y56W showed the largest absorptivity loss of ~ 100,000 M^{-1} cm^{-1}. The lower absorptivity for the hydrophobic substitutions may be due to a less favorable dipole moment in the excited state [41].

Φ_{fl} dropped significantly for all variants at position Y56, again except Y56H. The lower Φ_{fl} compensated for the loss in absorptivity and resulted in higher φP (3.4 to 6.9) than for wild-type smURFP (1.3). Mutants Y56L and Y56I showed comparable absorbance and quantum yield; however, the increase in PGE for Y56L resulted in a high φP of 6.9. To be able to probe the variants' photophysical behavior at wavelengths shorter than 680 nm and confirmed the results independently of MSOT, we record full spectra of wild-type smURFP and Y56L mutant using a custom-built OA spectrometer [24] (Figure 2D). The mutant showed approximately 50 % higher PGE when the two proteins were compared at their respective maxima of 645 and 675 nm. Based on equation (1), the decrease in Φ_{fl} between the mutant and wild-type protein can account for only 18% of this PGE increase. The bulk of this increase may be due to stabilization of the BV chromophore, which may reduce the likelihood of transient photoisomerization or other mechanisms of non-radiative energy dissipation effectively increasing PGE.

Position Y56 is clearly crucial for the photophysical characteristics of smURFP. This is somewhat surprising given the residue's orientation and its distance from the chromophore. The structure of smURFP-Y56R shows the distance between position 56 C_α and BV ring-A carbonyl to be ~ 6 Å[20]. However, position Y56 might interact with the chromophore via helix G, thus changes in Y56 may alter inter-helical packing, potentially also influencing the chromophore pocket. Moreover, our observation that relatively few of the tested binding pocket residues affect chromophore photophysics is surprising (Supplementary Table 1). This could be explained by the relatively large size of the chromophore binding cavity, which places the C_β of most lining residues at a considerable distance (mean 4.5 Å) from the chromophore. This makes it difficult to influence the chromophore through standard amino acid substitutions.

Our results illustrate the feasibility of improving PGE of covalent smURFP complexes in order to make them more suitable for optoacoustic imaging. We were able to substantially red-shift the absorption, making smURFP more compatible for *in vivo* imaging, and we improved PGE through a key mutation (Y56L) in the BV-binding pocket. Nevertheless, the best PGE among our mutants remains lower than that of the widely used fluorescent label iRFP720 [37]. This may reflect greater stabilization of the chromophore in iRFP720, which minimizes transient photoisomerization or other competitive photo-processes (except fluorescence). This highlights the central challenge for optimizing smURFP and other chromoprotein labels for optoacoustics: a less stabilized chromophore means lower Φ_{fl} and greater red shift, which increase OA signal; but it also means greater energy dissipation via competing pathways like isomerization, which decreases OA signal. It may be necessary to exhaustively search the mutational space of smURFP through high-throughput screening and directed evolution in order to strike a balance between these issues and thereby maximize optoacoustic performance.

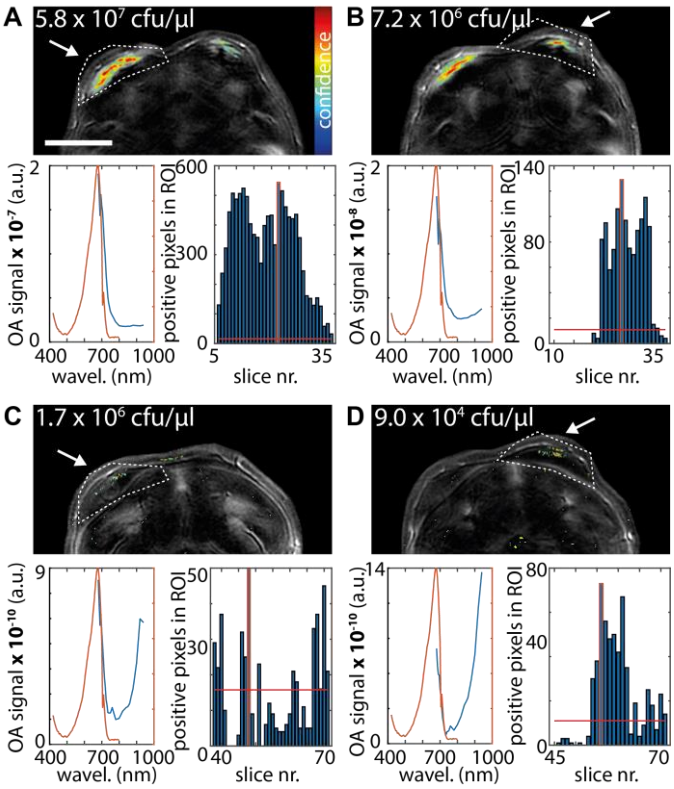

Figure 3: *In vivo* MSOT imaging of *E. coli* expressing smURFP-Y56L after injection in the back of a Fox-N1 nude mouse together with Matrigel. Reconstructed MSOT images (680 – 960 nm) are shown after unmixing for the spectra of smURFP-Y56L. Arrows indicate which side of the animal was injected. The concentration of injected bacteria is shown at the upper left of the MSOT images (injection volume was 30 µl). The colormap shows confidence in the unmixing, scaled separately for every image. The lower left panel shows the mean spectra of all positively unmixed pixels in the ROI (dotted line in the above image) in comparison with an OA spectrum of smURFP-Y56L protein (recorded with the OA spectrometer, 420 – 800 nm, arbitrarily scaled between 0 and 1. Note that the *y*-axis has different scale factors which inform about the signal intensity of the given bacteria number. The lower right panel shows number of positively unmixed pixels in consecutive slices. The slice shown in the image is boxed in orange. The red line indicates the number of positively unmixed pixels identifiable in a randomly chosen ROI (Supplementary Figure 9) in the mouse with no bacteria suspected (number of pixels is scaled to match ROI size). Scale bar is 0.5 mm.

Low chromophorylation of smURFP hamper it use in tracking mammalian cells in OA imaging[20,42]. In contrast, our mutants may prove suitable for OA imaging of bacteria injected into animal models, since smURFP is effectively chromophorylated in bacteria. Such imaging can be useful for studying concepts of bacterial tumor therapy [43] or to visualize bacterial infection [44]. To demonstrate that MSOT can resolve bacteria labeled with OA-optimized smURFP we chose variant smURFP-Y56L. After confirming superior

signal strength in the MSOT range in a blood phantom (Supplementary Figure 8) we injected different numbers of bacteria labeled with this variant into the back of a mouse. After recording MSOT data we used linear unmixing based on the spectra of the variants to identify regions showing smURFP-Y56L signal (Figure 3). Down to a concentration of $7.2x10^6$ cfu/μl regions with injected bacteria were identifiable with high confidence (Figure 3A-B). Lower concentrations led to clusters of pixels with a spectral signature similar to smURFP-Y56L in the regions where the bacteria were injected; however, the signals were similarly low as for false-positive unmixed pixels at uninjected sites (Supplementary Figure 9). smURFP-Y56L and other variants analyzed by us [20] behave as a dimer in solution similar to smURFP wild-type (Supplementary Figure 10) similarly the resistance of smURFP-Y56L to photobleaching under OA illumination proved to be similar to that of wild-type smURFP and iRFP720 (Supplementary Figure 11). Our data show that small populations of bacteria expressing smURFP variants can be identified *in vivo* adding a further label to the growing catalogue of OA-ready label proteins which opens up possibilities of spectral multiplexing also in OA.

CONCLUSION

Here we demonstrate the feasibility of improving the optoacoustic performance of smURFP through structure-based mutagenesis. We studied mutant smURFP covalently and non-covalently bound to BV and identified major positions influencing their spectral properties as well as their PGE. The residue positions identified here may pave the way for further engineering of PBPs for optoacoustics. Such developments might focus on the recently introduced BDFP [18], which has a Met at the position equivalent to Y56 in smURFP. BDFP is shifted more to the red than smURFP but shows lower molar absorption. Moreover, insight gained on studying interactions that foster OA signal generation in context with BV chromophores will also benefit further engineering of the emerging class of photo-controllable bacteriophytochromes[15,45–48].

SUPPORTING INFORMATION

The Supporting Information is available free of charge on the ACS Publications website at DOI: XX.XXXX/acs.chem-bio.XXXXXXX. Supporting Information contains Supplementary Figures as indicated in the manuscript.

AUTHOR INFORMATION

Corresponding Author

*E-mail: andre.stiel@helmholtz-muenchen.de.

AUTHOR CONTRIBUTIONS

J.P.F-W. and A.C.S. conceived experiments, analyzed all data and wrote the manuscript. V.N. and A.C. contributed to the manuscript. J.P.F-W., K.M. and S.G. conducted molecular biology and protein purification, spectroscopy and optoacoustic experiments. J.P.F-W., P.V. and Y.H. built the optoacoustic spectrometer. K.R. conducted and analyzed analytical ultracentrifugation experiments.

V.N. is a shareholder of iThera, manufacturer of the MSOT device in this study. The other authors declare no competing financial interests.

ACKNOWLEDGMENTS

The authors wish to thank R. Hillermann and U. Klemm for technical assistance, and A. Rodríguez and M. Flores for discussions on the manuscript. A.C.S. and K.M. received support from the Deutsche Forschungsgemeinschaft (STI 656/1-1). Y.H. received support from DFG (NT 3/9-1, NT 3/10-1) and CSC (201306960006). Parts of this work (OA spectrometer) received funding Ministry of Education and Research, Photonic Science Germany, Tech2See-13N12624, 13N12623.

REFERENCES

(1) Oraevsky, A. A.; Jacques, S. L.; Tittel, F. K. Measurement of Tissue Optical Properties by Time-Resolved Detection of Laser-Induced Transient Stress. *Appl. Opt.* **1997**, *36*, 402–415.
(2) Wang, L. V.; Hu, S. Photoacoustic Tomography: In Vivo Imaging from Organelles to Organs. *Science.* **2012**, *335*, 1458–1462.
(3) Taruttis, A.; Ntziachristos, V. Advances in Real-Time Multispectral Optoacoustic Imaging and Its Applications. *Nat. Phot.* **2015**, *9*, 219–227.
(4) Rosencwaig, A. Photoacoustic Spectroscopy. *Annu. Rev. Biophys. Bioeng.* **1980**, *9*, 31–54.
(5) Brunker, J.; Yao, J.; Laufer, J.; Bohndiek, S. E. Photoacoustic Imaging Using Genetically Encoded Reporters: A Review. *J. Biomed. Opt.* **2017**, *22*, 070901.
(6) Braslavsky, S. E.; Ellul, R. M.; Weiss, R. G.; Al-Ekabi, H.; Schaffner, K. Photoprocesses in Biliverdin Dimethyl Ester in Ethanol Studied by Laser-Induced Optoacoustic Spectroscopy (Lioas). *Tetrahedron* **1983**, *39*, 1909–1913.
(7) Ripoll, J.; Koberstein-Schwarz, B.; Ntziachristos, V. Unleashing Optics and Optoacoustics for Developmental Biology. *Trends Biotechnol.* **2015**, *33*, 679–691.
(8) Wang, L. V; Gao, L. Photoacoustic Microscopy and Computed Tomography: From Bench to Bedside. *Annu. Rev. Biomed. Eng.* **2014**, *16*, 155–185.
(9) Paproski, R. J.; Forbrich, A. E.; Wachowicz, K.; Hitt, M. M.; Zemp, R. J. Tyrosinase as a Dual Reporter Gene for Both Photoacoustic and Magnetic Resonance Imaging. *Biomed. Opt. Express* **2011**, *2*, 771–780.
(10) Li, L.; Zemp, R. J.; Lungu, G.; Stoica, G.; Wang, L. V. Photoacoustic Imaging of LacZ Gene Expression in Vivo. *J. Biomed. Opt.* **2013**, *12*, 020504.
(11) Jiang, Y.; Sigmund, F.; Reber, J.; Luís Deán-Ben, X.; Glasl, S.; Kneipp, M.; Estrada, H.; Razansky, D.; Ntziachristos, V.; Westmeyer, G. G. Violacein as a Genetically-Controlled, Enzymatically Amplified and Photobleaching-Resistant Chromophore for Optoacoustic Bacterial Imaging. *Sci. Rep.* **2015**, *5*, 11048.

(12) Li, Y.; Forbrich, A.; Wu, J.; Shao, P.; Campbell, R. E.; Zemp, R. Engineering Dark Chromoprotein Reporters for Photoacoustic Microscopy and FRET Imaging. *Sci. Rep.* **2016**, *6*, 22129.
(13) Filonov, G. S.; Krumholz, A.; Xia, J.; Yao, J.; Wang, L. V.; Verkhusha, V. V. Deep-Tissue Photoacoustic Tomography of a Genetically Encoded near-Infrared Fluorescent Probe. *Angew. Chem. Int. Ed. Engl.* **2012**, *51*, 1448–1451.
(14) Märk, J.; Dortay, H.; Wagener, A.; Zhang, E.; Buchmann, J.; Grötzinger, C.; Friedrich, T.; Laufer, J. Dual-Wavelength 3D Photoacoustic Imaging of Mammalian Cells Using a Photoswitchable Phytochrome Reporter Protein. *Commun. Phys.* **2018**, *1*, 3.
(15) Yao, J.; Kaberniuk, A. A.; Li, L.; Shcherbakova, D. M.; Zhang, R.; Wang, L. V. L. L. V; Li, G.; Verkhusha, V. V.; Wang, L. V. L. L. V. Multiscale Photoacoustic Tomography Using Reversibly Switchable Bacterial Phytochrome as a Near-Infrared Photochromic Probe. *Nat. Methods* **2015**, *13*, 1–9.
(16) Watanabe, M.; Ikeuchi, M. Phycobilisome: Architecture of a Light-Harvesting Supercomplex. *Photosynth. Res*. 2013, 265–276.
(17) Rodriguez, E. A.; Tran, G. N.; Gross, L. A.; Crisp, J. L.; Shu, X.; Lin, J. Y.; Tsien, R. Y. A Far-Red Fluorescent Protein Evolved from a Cyanobacterial Phycobiliprotein. *Nat. Methods* **2016**, *13*, 763–769.
(18) Ding, W.; Miao, D.; Hou, Y.; Jiang, S.; Zhao, B.; Zhou, M.; Scheer, H.; Zhao, K. Small Monomeric and Highly Stable Near-Infrared Fl Uorescent Markers Derived from the Thermophilic Phycobiliprotein , ApcF2. *BBA - Mol. Cell Res.* **2017**, *1864*, 1877–1886.
(19) Rumyantsev, K. A.; Shcherbakova, D. M.; Zakharova, N. I.; Emelyanov, A. V.; Turoverov, K. K.; Verkhusha, V. V. Minimal Domain of Bacterial Phytochrome Required for Chromophore Binding and Fluorescence. *Sci. Rep.* **2015**, *5*, 18348.
(20) Fuenzalida-Werner, J. P.; Janowski, R.; Mishra, K.; Weidenfeld, I.; Niessing, D.; Ntziachristos, V.; Stiel, A. C. Crystal Structure of a Biliverdin-Bound Phycobiliprotein: Interdependence of Oligomerization and Chromophorylation. *J. Struct. Biol.* **2018**.
(21) Shu, X.; Royant, A.; Lin, M. Z.; Aguilera, T. A.; Lev-Ram, V.; Steinbach, P. A.; Tsien, R. Y. Mammalian Expression of Infrared Fluorescent Proteins Engineered from a Bacterial Phytochrome. *Science.* **2009**, *324*, 804–807.
(22) Ho, C. J. H.; Balasundaram, G.; Driessen, W.; McLaren, R.; Wong, C. L.; Dinish, U. S.; Attia, A. B. E.; Ntziachristos, V.; Olivo, M. Multifunctional Photosensitizer-Based Contrast Agents for Photoacoustic Imaging. *Sci. Rep.* **2015**, *4*, 5342.
(23) Song, K. H.; Stein, E. W.; Margenthaler, J. A.; Wang, L. V. Noninvasive Photoacoustic Identification of Sentinel Lymph Nodes Containing Methylene Blue in Vivo in a Rat Model. *J. Biomed. Opt. 13*, 054033.
(24) Vetschera, P.; Mishra, K.; Fuenzalida-Werner, J. P.; Chmyrov, A.; Ntziachristos, V.; Stiel, A. C. Characterization of Reversibly Switchable Fluorescent Proteins in Optoacoustic Imaging. *Anal. Chem.* **2018**, *90*, 10527–10535.
(25) Rosenthal, A.; Razansky, D.; Ntziachristos, V. Fast Semi-Analytical Model-Based Acoustic Inversion for Quantitative Optoacoustic Tomography. *IEEE Trans. Med. Imaging* **2010**, *29*, 1275–1285.
(26) Peng, P.-P.; Dong, L.-L.; Sun, Y.-F.; Zeng, X.-L.; Ding, W.-L.; Scheer, H.; Yang, X.; Zhao, K.-H. The Structure of Allophycocyanin B from Synechocystis PCC 6803 Reveals the Structural Basis for the Extreme Redshift of the Terminal Emitter in Phycobilisomes. *Acta Crystallogr. Sect. D* **2014**, *70*, 2558–2569.
(27) Apt, K. E.; Collier, J. L.; Grossman, A. R. Evolution of the Phycobiliproteins. *J. Mol. Biol.* **1995**, *248*, 79–96.

(28) Scheer, H.; Zhao, K.-H. H. Biliprotein Maturation: The Chromophore Attachment. *Mol. Microbiol.* **2008**, *68*, 263–276.
(29) Miao, D.; Ding, W. L.; Zhao, B. Q.; Lu, L.; Xu, Q. Z.; Scheer, H.; Zhao, K. H. Adapting Photosynthesis to the Near-Infrared: Non-Covalent Binding of Phycocyanobilin Provides an Extreme Spectral Red-Shift to Phycobilisome Core-Membrane Linker from Synechococcus Sp. PCC7335. *Biochim. Biophys. Acta - Bioenerg.* **2016**, *1857*, 688–694.
(30) Hontani, Y.; Shcherbakova, D. M.; Baloban, M.; Zhu, J.; Verkhusha, V. V; Kennis, J. T. M. Bright Blue-Shifted Fluorescent Proteins with Cys in the GAF Domain Engineered from Bacterial Phytochromes: Fluorescence Mechanisms and Excited-State Dynamics. *Sci. Rep.* **2016**, *6*, 37362.
(31) Yang, L.; Adam, C.; Cockroft, S. L. Quantifying Solvophobic Effects in Nonpolar Cohesive Interactions. *J. Am. Chem. Soc.* **2015**, *137*, 10084–10087.
(32) Fuenzalida, J. P.; Flores, M. E.; Móniz, I.; Feijoo, M.; Goycoolea, F.; Nishide, H.; Moreno-Villoslada, I. Immobilization of Hydrophilic Low Molecular-Weight Molecules in Nanoparticles of Chitosan/Poly(Sodium 4-Styrenesulfonate) Assisted by Aromatic-Aromatic Interactions. *J. Phys. Chem. B* **2014**, *118*, 9782–9791.
(33) Novotná, P.; Králík, F.; Urbanová, M. Chiral Recognition of Bilirubin and Biliverdin in Liposomes and Micelles. *Biophys. Chem.* **2015**, *205*, 41–50.
(34) Blauer, G.; Wagniere, G. Conformation of Bilirubin and Biliverdin in Their Complexes with Serum Albumin. *J. Am. Chem. Soc.* **1975**, *97*, 1949–1954.
(35) Deán-Ben, X. L.; Gottschalk, S.; Mc Larney, B.; Shoham, S.; Razansky, D. Advanced Optoacoustic Methods for Multiscale Imaging of in Vivo Dynamics. *Chem. Soc. Rev.* **2017**, *46*, 2158–2198.
(36) Laufer, J.; Jathoul, A.; Pule, M.; Beard, P. In Vitro Characterization of Genetically Expressed Absorbing Proteins Using Photoacoustic Spectroscopy. *Biomed. Opt. Express* **2013**, *4*, 2477–2490.
(37) Shcherbakova, D. M.; Verkhusha, V. V. Near-Infrared Fluorescent Proteins for Multicolor in Vivo Imaging. *Nat. Methods* **2013**, *10*, 751–754.
(38) Aveline, B. M.; Hasan, T.; Redmond, R. W. The Effects of Aggregation, Protein Binding and Cellular Incorporation on the Photophysical Properties of Benzoporphyrin Derivative Monoacid Ring A (BPDMA). *J. Photochem. Photobiol. B Biol.* **1995**, *30*, 161–169.
(39) Bhasikuttan, A. C.; Mohanty, J.; Nau, W. M.; Pal, H. Efficient Fluorescence Enhancement and Cooperative Binding of an Organic Dye in a Supra-Biomolecular Host-Protein Assembly. *Angew. Chemie - Int. Ed.* **2007**, *46*, 4120–4122.
(40) Tiago D. Martins, Marlene L. Pacheco, Renato E. Boto, Paulo Almeida, José Paulo S. Farinha, L. V. R. Synthesis, Characterization and Protein-Association of Dicyanomethylene Squaraine Dyes. *Dye. Pigment.* **2017**, *147*, 120–129.
(41) Hilborn, R. C. Einstein Coefficients, Cross Sections, f Values, Dipole Moments, and All That. *Am. J. Phys.* **1982**, *50*, 982–986.
(42) Shemetov, A. A.; Oliinyk, O. S.; Verkhusha, V. V. How to Increase Brightness of Near-Infrared Fluorescent Proteins in Mammalian Cells. *Cell Chem. Biol.* **2017**, *24*, 758-766.
(43) Zhou, S.; Gravekamp, C.; Bermudes, D.; Liu, K. Tumour-Targeting Bacteria Engineered to Fight Cancer. *Nat. Rev. Cancer* **2018**, *18*, 727–743.
(44) Luker, K. E.; Luker, G. D. Bioluminescence Imaging of Reporter Mice for Studies of Infection and Inflammation. *Antiviral Res.* **2010**, *86*, 93–100.
(45) Vetschera, P.; Mishra, kanuj; Fuenzalida Werner, J.-P.; Chmyrov, A.; Ntziachristos, V.; Stiel, A. C. Characterization of Reversibly Switchable Fluorescent Proteins (RsFPs) in

Optoacoustic Imaging. *Anal. Chem.* **2018,** 90, 10527-10535.
(46) Li, L.; Shemetov, A. A.; Baloban, M.; Hu, P.; Zhu, L.; Shcherbakova, D. M.; Zhang, R.; Shi, J.; Yao, J.; Wang, L. V.; Verkhusha V.V. Small Near-Infrared Photochromic Protein for Photoacoustic Multi-Contrast Imaging and Detection of Protein Interactions in Vivo. *Nat. Commun.* **2018**, *9*, 2734.
(47) Dortay, H.; Märk, J.; Wagener, A.; Zhang, E.; Grötzinger, C.; Hildebrandt, P.; Friedrich, T.; Laufer, J. Dual-Wavelength Photoacoustic Imaging of a Photoswitchable Reporter Protein; Oraevsky, A. A., Wang, L. V., Eds.; International Society for Optics and Photonics, 2016; Vol. 9708, 970820.
(48) Chee, R. K. W.; Li, Y.; Zhang, W.; Campbell, R. E.; Zemp, R. J. In Vivo Photoacoustic Difference-Spectra Imaging of Bacteria Using Photoswitchable Chromoproteins. *J. Biomed. Opt.* **2018**, *23*, 1–11.